D

EGYPTIAN ACADEMIC JOURNAL OF

BIOLOGICAL SCIENCES

HISTOLOGY & HISTOCHEMISTRY

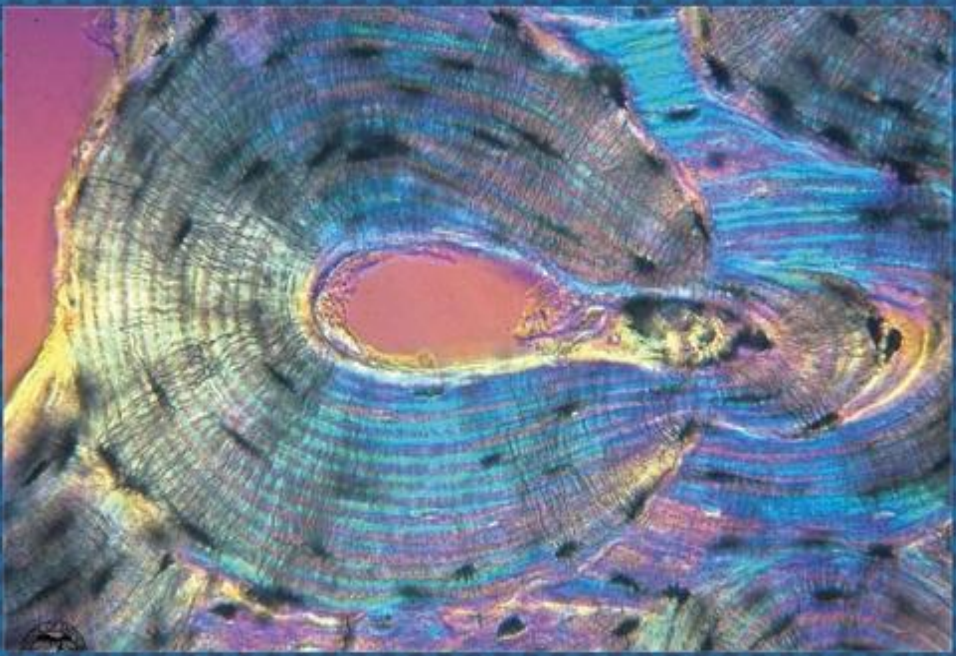

ISSN
2090-0775

WWW.EAJBS.EG.NET

Vol. 17 No. 2 (2025)

Citation: Egypt*. Acad. J. Biolog. Sci. (D-Histology and histochemistry) Vol.17(2) pp61-85(2025)*
DOI: 10.21608/EAJBSD.2025.453479

Egypt. Acad. J. Biolog. Sci., 17(2):61-85 (2025)

Egyptian Academic Journal of Biological Sciences
D. Histology & Histochemistry
ISSN 2090 – 0775
http://eajbsd.journals.ekb.eg

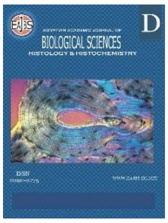

Possible Role of Empagliflozin in Ameliorating Structural Changes of the Renal Cortex Caused by Alloxan-Induced Diabetes in Adult Male Albino Rats

Reneah R. Bushra
Human Anatomy and Embryology Department, Faculty of Medicine, Assiut University, Assiut, Egypt.
E-mail : reneah@aun.edu.eg

ARTICLE INFO
Article History
Received:7/8/2025
Accepted:16/9/2025
Available:20/9/2025

***Keywords*:**
Renal Cortex;
Alloxan-induced Diabetes;
Empagliflozin;
Albino Rats.

ABSTRACT

Background: The renal cortex plays a chief role in blood filtration. Diabetic patients are at risk of developing kidney disease. Empagliflozin is efficient in lowering blood glucose levels. **The work aimed to** evaluate empagliflozin in ameliorating renal cortical changes caused by alloxan-induced diabetes. **Material and methods:** 24 adult male albino rats, aged three months, weighing 200-250 g, were randomly, equally divided into 4 groups. Group I (control group), received no treatment, group II (sham group) received 10 mg empagliflozin/kg b.w./day, orally via gavage for 8 weeks, group III (diabetic group) received a single intraperitoneal injection of 150 mg alloxan/kg b.w., and group IV (DM+Empagliflozin-treated group) received 10 mg empagliflozin/kg b.w./day, orally via gavage for 8 weeks, starting two days after induction of diabetes by a single intraperitoneal injection of 150 mg alloxan/kg b.w. At the designated time, all rats were anaesthetized, sacrificed, and the kidneys were extracted and processed for histological, immunohistochemical, and morphometric studies. **Results:** The diabetic group revealed a mixture of hypertrophied and degenerated glomeruli, thickened glomerular basement membrane, tubular degeneration, a significant decrease in area % and optical density of connexin-43 and Nrf2 immunoreactivity, and a significant increase in area % of PAS, Masson's trichrome, and Sirius red staining, as well as area % and optical density of caspase-3 immunoreactivity in comparison to the control. Empagliflozin ameliorated these changes. **Conclusion:** Alloxan-induced diabetes exerts deleterious effects on the renal cortex. Empagliflozin ameliorated these alterations, likely by suppressing fibrosis, inflammation, apoptosis, and oxidative stress, while enhancing intercellular communication.

INTRODUCTION

The renal cortex is the outer region of the kidney located between the renal capsule and the renal medulla. It extends inward as renal columns between the pyramids of the medulla (Chew & Schenck, 2023). The cortex plays a central role in filtration, reabsorption, and secretion. This is attributed to its abundance of key structures, including the renal corpuscles (Gartner & Lee, 2024). At the urinary pole of the renal corpuscle, the proximal convoluted tubules reabsorb all glucose, amino acids, and small proteins, along with 60–80% of sodium chloride and water, returning them to the peritubular capillary system. The distal convoluted tubules reabsorb Na^+ from the filtrate and actively transport it into the renal interstitium, while also secreting K^+, NH_4^+, and H^+ from the interstitium into the filtrate (Chew & Schenck, 2023).

Citation: Egypt. *Acad. J. Biolog. Sci. (D-Histology and histochemistry) Vol.17(2) pp61-85(2025)*
DOI: 10.21608/EAJBSD.2025.453479

Diabetes mellitus (DM) is a metabolic disorder characterized by hyperglycemia resulting from a defect in insulin secretion and action. DM exerts widespread systemic effects, leading to progressive damage in multiple organs (Ahmed *et al.,* 2023).

These alterations induce microvascular complications, particularly in the kidneys, leading to diabetic nephropathy (DN) (Alqudah *et al.,* 2024). DN is a serious and progressive complication of diabetes that advances to end-stage renal disease. Despite global efforts to manage DN, the number of diabetic patients requiring dialysis has more than doubled in recent decades and continues to rise steadily. This highlights the importance of early intervention and tight glycemic control to prevent irreversible kidney dysfunction (Hsu *et al.,* 2024).

Animal models, particularly albino rats, provide a controlled platform for investigating tissue-level changes and drug-induced modulation (Kumar *et al.,* 2025). Alloxan is a widely used agent for inducing a diabetes-like state in animals, particularly type-1 diabetes mellitus, as reported by Amer *et al.* (2022). They referred that alloxan generates reactive oxygen species (ROS) that selectively destroy the insulin-producing β-cells of the pancreatic islets, leading to insulin deficiency and persistent hyperglycemia.

Effective therapies to prevent or reverse diabetes-induced kidney injury remain limited (Hsu *et al.,* 2024). Currently, empagliflozin, a sodium-glucose cotransporter-2 (SGLT2) inhibitor, is approved by the Food and Drug Administration for the management of type 2 diabetes mellitus due to its proven efficacy in improving glycemic control (Jha *et al.,* 2024). Emerging evidence suggests that some of their benefits, such as anti-fibrotic and anti-inflammatory effects, may be independent of their glucose-lowering action (Huang *et al.,* 2024 and Fayed *et al.,* 2025). Badreldin *et al.* (2024) referred to the use of empagliflozin in protection against atrial fibrillation-induced acute kidney injury in rats, and Colbert *et al.* (2023), Groyer *et al.* (2024), and Fayed *et al.* (2025) in the treatment of patients with chronic kidney disease.

Therefore, the present study aimed to evaluate the histological, immunohistochemical, and morphometric renal cortical alterations induced by alloxan-induced diabetes in adult male albino rats, and to assess the potential ameliorative effects of empagliflozin in this disease model.

MATERIALS AND METHODS

Drug Preparation and Administration:

Empacosa/Empagliflozin was obtained in white-colored, coated tablets (ZETA PHARMA® Company, Egypt, CAS number: 864070-44-0). Each tablet contained 10 mg of empagliflozin. The tablets were crushed and dissolved in distilled water to prepare a homogeneous suspension. It was freshly prepared each day. The drug was administered orally using a gavage needle at a dose of 10 mg/kg b.w., daily for 8 consecutive weeks (Li *et al.,* 2019).

Induction of Diabetes Mellitus:

Alloxan monohydrate powder (CAS number: 2244-11-3) was derived from Sigma-Aldrich, Inc., St. Louis, Missouri, USA. Following a 12-hour fasting period, the animals were once injected intraperitoneally with 150 mg alloxan/kg b.w., freshly dissolved in sterile 0.9% saline (Amer *et al.,* 2022). To reduce the risk of acute hypoglycemia due to sudden insulin release, the rats were given a 10% glucose solution for 24 hours post-alloxan injection (Misra & Aiman, 2012). The occurrence of diabetes was assessed by measuring random blood glucose levels using a glucometer at 72 hours and one week after alloxan injection. Rats exhibiting blood glucose levels greater than 200 mg/dL were considered diabetic and included in the study (Amer *et al.,* 2022).

Experimental Animals and Design:

A total of 24 adult male albino rats (3 months old, weighing 200-250 g) were provided from the Animal House of the Faculty of Medicine, Assiut University. The animals were housed under standard laboratory conditions of the light/dark cycle and temperature, with free access to food and water ad libitum for one week of acclimatization before the experiment.

Subsequently, the animals were randomly divided into four equal groups (6 rats/group). Group I (control group) received no treatment, Group II (sham group) received 10 mg empagliflozin/kg b.w./day, orally via gavage for 8 weeks. Group III (diabetic group) received a single intraperitoneal injection of 150 mg alloxan/kg b.w. (Amer *et al.,* 2022). Group IV (DM+Empagliflozin-treated group) received 10 mg empagliflozin/kg b.w./day, orally via gavage for 8 weeks, starting two days after induction of diabetes by a single intraperitoneal injection of 150 mg alloxan/kg b.w. (Li *et al.,* 2019).

All procedures were conducted following ethical guidelines for animal research and were fully approved by the Institutional Animal Care and Use Committee and by the Institutional Review Board of the Faculty of Medicine, Assiut University (Approval No. 04-2025-300652).

1. Histological Study

At the designated time, the rats were anesthetized with either inhalation, followed by intracardiac perfusion of 0.9% saline through the left ventricle. They were then euthanized by cervical dislocation. Immediately after sacrifice, the kidneys were carefully excised. The right kidneys were dissected and fixed in 10% buffered formalin for 24-48 h, dehydrated in graded alcohols, cleared in xylene, and embedded in paraffin for light microscopy. Paraffin blocks were sectioned at 8-10 µm and stained with hematoxylin and eosin (H&E) to demonstrate the general tissue architecture. Periodic Acid-Schiff (PAS) was used to assess the integrity and thickness of the glomerular and tubular basement membranes, mesangial matrix, and brush borders of the proximal convoluted tubules. Other sections were stained with Masson's trichrome to detect collagen fiber deposition. Sirius red stain was performed to differentiate and quantify collagen, particularly types I and III, which are key indicators of fibrosis (Suvarna *et al.,* 2012).

The left kidneys were dissected and fixed in 2.5% glutaraldehyde (in 0.1 M phosphate buffer, pH 7.4). For scanning electron microscopy (SEM), samples (5 × 5 mm²) were post-fixed in 1% osmium tetroxide and dehydrated through an ascending ethanol series. Critical point drying was performed using liquid carbon dioxide, and the samples were mounted on metallic stubs with silver paint. They were then gold-coated to a thickness of 15 nm using a sputter coating apparatus according to Heikal *et al.* (2024). Then, they were examined and photographed by a JEOL (JSM-5400 LV) scanning electron microscope at the Electron Microscopy Unit, Assiut University. According to Suvarna *et al.* (2012), semithin sections (1 µm) were prepared and stained with Toluidine blue to assess cellular details and ultrathin sections (70-90 nm) were obtained using an ultramicrotome, stained with uranyl acetate and lead citrate, and subsequently examined and photographed by a JEOL (JEM-100 CX-II, Tokyo, Japan) transmission electron microscope at the Electron Microscopy Unit, Assiut University.

2. Immunohistochemical Study:

Immunohistochemical techniques were applied to formalin-fixed, paraffin-embedded tissue sections, which were mounted on positively charged slides, then deparaffinized and rehydrated. Antigen retrieval was carried out using citrate buffer (pH 6.0), and endogenous peroxidase activity was inhibited with 3% hydrogen peroxide. The sections were incubated with primary antibodies against caspase-3 (apoptosis marker), connexin-43 (marker of gap junction integrity and intercellular communication), and Nrf2 (nuclear factor erythroid 2-related factor 2; oxidative stress response marker). After incubation with the appropriate secondary antibodies, the reaction was visualized using 3,3′-diaminobenzidine (DAB), followed by hematoxylin counterstaining, as described by Suvarna *et al.* (2012), Ahmed *et al.* (2022), Barakat *et al.* (2022), and El-Shafei *et al.* (2023).

3. Morphometric Study:

H&E-stained sections at ×100 magnification were analyzed to determine the number of cortical nephrons within a fixed area of 0.38 mm^2. Toluidine blue-stained sections at ×100 magnification were examined to measure the total glomerular capillary tuft surface area per glomerulus and the epithelial height of the proximal and distal convoluted tubules. TEM photomicrographs at ×14000 magnification were evaluated to measure glomerular basement membrane (GBM) thickness, defined as the distance between the basal aspect of the endothelial membrane and the basal aspect of the podocyte membrane in contact with the GBM, according to Viana *et al.* (2022).

The surface area % of PAS, Masson's trichrome, and Sirius red stains, as well as caspase-3, connexin-43, and Nrf2 immunoreactivity in the renal cortex, was quantified to evaluate the extent of both staining and immunoreactivity according to Kler *et al.* (2022). In addition, the optical density of caspase-3, connexin-43, and Nrf2 immunoreactivity was measured in all experimental groups to assess the intensity of immune reactions according to Jovanovic *et al.* (2021).

The measurements were done using ImageJ software (version 1.54p). The parameters were measured in ten non-overlapping fields for each animal in each studied group.

Statistical Analysis:

The data were expressed as mean ± standard deviation (SD). Statistical analysis was conducted using SPSS software (IBM SPSS Statistics, version 31.0; IBM Corp., Chicago, IL, USA). Normality was assessed with the Kolmogorov-Smirnov and Shapiro-Wilk tests, which confirmed that the data were normally distributed. Comparisons among studied groups were performed using one-way analysis of variance (ANOVA), followed by Tukey's post hoc test for pairwise comparisons. All tests were two-tailed, and a p-value $\leq$ 0.05 was considered statistically significant (Korkmaz & Demir, 2023).

RESULTS

I- Biochemical Results:

There was no significant difference in random blood glucose levels between the control and sham groups. The diabetic group exhibited significantly higher blood glucose levels compared to the control group. In contrast, no significant difference was observed between the blood glucose levels of the DM+Empagliflozin-treated group and the control group (Table 1).

Table 1: Random blood glucose levels of the studied groups.

	Control group	Sham group	Diabetic group	DM+Empagliflozin-treated group
Blood glucose level [mg/dL]	90.89±4.5	91.56±6.2	314.30±8.67***	104.20±7.53

Results were expressed as mean ± SD

***Differences at $p < 0.001$ in comparison to the control

II- Morphometric Results:

There were no significant differences in morphometric results between the control and sham groups throughout the experiment. In the diabetic group, there was a statistically significant decrease in the number of cortical nephrons per fixed area of 0.38 mm^2, total glomerular capillary tuft surface area per glomerulus, and epithelial height of the proximal and distal convoluted tubules, accompanied by a significant increase in glomerular basement membrane thickness compared to the control. In contrast, no significant differences were observed in the DM+ Empagliflozin-treated group relative to the control (Table 2, Histogram 1). The surface area % of PAS, Masson's trichrome, and Sirius red stains was significantly increased in the diabetic group compared to the control. No significant differences were observed in the DM+Empagliflozin-treated group compared to the control (Table 3, Histogram 2). Similarly, the surface area % and optical density of caspase-3 immunoreactivity were significantly increased in the diabetic group relative to the control. Conversely, connexin-43 and Nrf2 immunoreactivity showed a significant decrease in both surface area % and optical density in the diabetic group. No significant differences were noted in the DM+Empagliflozin-treated group compared to the control (Tables 4 and 5, Histogram 2).

Table 2: Number of cortical nephrons per fixed area of 0.38 mm², glomerular basement membrane thickness, total glomerular capillary tuft surface area per glomerulus, and epithelial height of the proximal and distal convoluted tubules in the studied groups.

	Control group	**Sham group**	**Diabetic group**	**DM+Empagliflozin-treated group**
Number of cortical nephrons/0.38 mm²	7.5±0.52	7.47±0.12	6.1±0.67**	7.2±0.63
Glomerular basement membrane thickness (nm)	424.7±14.17	430.7±18.86	764.5±27.73***	450.4±29.73
Total glomerular capillary tuft surface area/glomerulus (µm²)	3755±153.56	3750±767.56	1596±71.83***	3675±120.76
Epithelial height of the proximal convoluted tubules (µm)	22.1±1.66	21.98±2.14	14.5±1.26***	20.8±1.81
Epithelial height of the distal convoluted tubules (µm)	12.2±1.75	12.25±0.98	6.9±0.73***	11.2±1.75

Results were expressed as mean ± SD
**Differences at $p < 0.01$ in comparison to the control
***Differences at $p < 0.001$ in comparison to the control

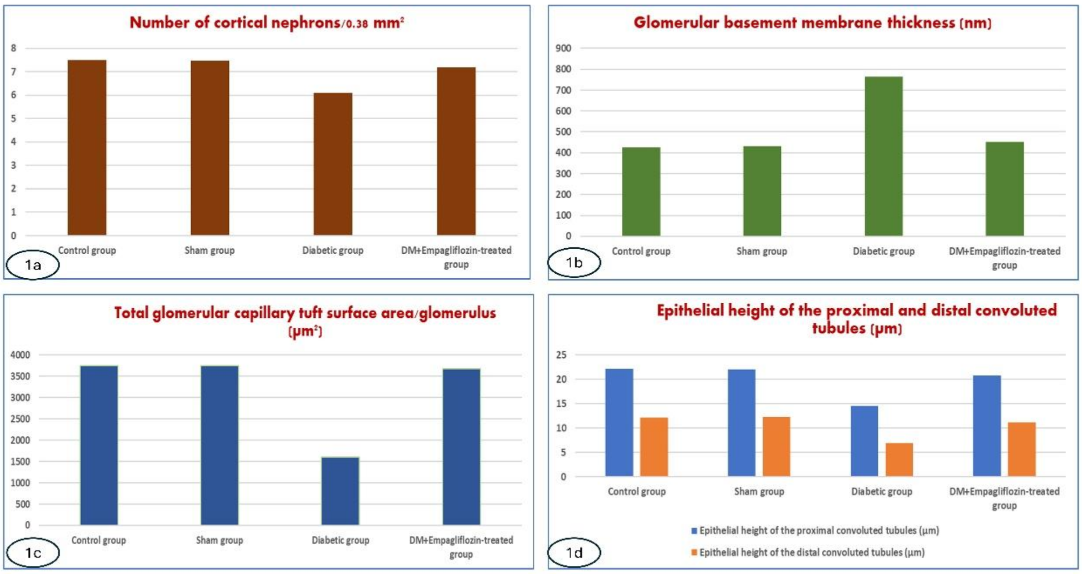

Histogram 1 showing (a): the number of cortical nephrons per fixed area, (b): the glomerular basement membrane thickness, (c): the total glomerular capillary tuft surface area per glomerulus, and (d): the epithelial height of the proximal and distal convoluted tubules of the studied groups.

Table 3: The surface area % of the PAS, Masson’s trichrome, and Sirius red stains of the renal cortex of the studied groups.

	Control group	Sham group	Diabetic group	DM+Empagliflozin-treated group
Surface area % of PAS stain	4.21±0.2	4.18±0.76	8.83±0.42***	4.53±0.18
Surface area % of Masson’s trichrome stain	6.36±0.23	6.2±0.34	18.59±0.45***	6.64 ±0.18
Surface area % of Sirius red stain	1.87±0.01	1.88±0.07	8.79±0.02***	1.88±0.09

Results were expressed as mean ± SD
***Differences at $p < 0.001$ in comparison to the control

Table 4: The surface area % of the caspase-3, connexin-43, and Nrf2 immunoreactivity of the renal cortex of the studied groups

	Control group	Sham group	Diabetic group	DM+Empagliflozin-treated group
Surface area % of caspase-3 immunoreactivity	1.03±0.01	1.04±0.07	5.25±0.16***	1.07±0.03
Surface area % of connexin-43 immunoreactivity	1.72±0.01	1.71±0.09	0.76±0.15***	1.69±0.01
Surface area % of Nrf2 immunoreactivity	5.71±0.38	5.69±0.23	0.62±0.25***	5.28±0.26

Results were expressed as mean ± SD
***Differences at $p < 0.001$ in comparison to the control

Table 5: The optical density of the caspase-3, connexin-43, and Nrf2 immunoreactivity of the renal cortex of the studied groups

	Control group	Sham group	Diabetic group	DM+Empagliflozin-treated group
Optical density of caspase-3 immunoreactivity	0.19±0.01	0.19±0.87	0.33±0.02***	0.2±0.01
Optical density of connexin-43 immunoreactivity	0.23±0.01	0.24±0.11	0.18±0.01***	0.22±0.02
Optical density of Nrf2 immunoreactivity	0.36±0.02	0.35±0.36	0.16±0.01***	0.33±0.01

Results were expressed as mean ± SD
***Differences at $p < 0.001$ in comparison to the control

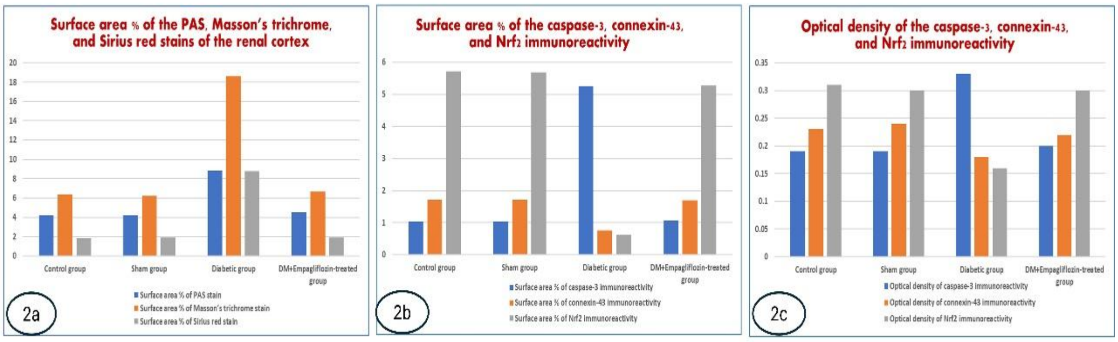

Histogram 2: showing (a): the surface area % of the PAS, Masson’s trichrome, and Sirius red stains, (b): the surface area % of the caspase-3, connexin-43, and Nrf2 immunoreactivity, and (c): the optical density of the caspase-3, connexin-43, and Nrf2 immunoreactivity of the renal cortex of the studied groups.

III- Histological Results:

There were no obvious differences in the histological findings between the control and sham groups throughout the experiment. Therefore, only photomicrographs of the control group were included.

1- Light Microscopic Results:

1.1. Hematoxylin and Eosin Staining:

The hematoxylin and eosin-stained control renal cortical sections showed renal corpuscles and tubules. The corpuscles consisted of glomeruli enclosed by Bowman's capsule. Bowman's spaces were clearly delineated between the parietal layer and the glomeruli. The parietal layer was composed of simple squamous epithelium, while the visceral layer exhibited podocytes. The glomerular capillaries were lined by endothelial cells. Intraglomerular mesangial cells and matrix were observed between the capillary loops. Extraglomerular mesangial cells and the macula densa were also identified. The proximal convoluted tubules exhibited a narrow lumen and were lined by darkly stained cuboidal epithelial cells with rounded, basally located nuclei and a prominent brush border. In contrast, the distal convoluted tubules had a wider lumen and were lined by lightly stained cuboidal cells with centrally located nuclei and lacked a brush border (Figs. 1a, 1d, 1g).

In the diabetic group, glomeruli exhibited a mixture of hypertrophied and degenerated glomeruli. The parietal layer of Bowman's capsule was thickened and composed of cuboidal cells. Desquamated cells were observed within the dilated Bowman's space. Podocytes were scanty. Glomerular capillaries were engorged with blood and lined by endothelial cells exhibiting pyknotic nuclei. Intraglomerular mesangial cells and matrix were intensely stained. The nuclei of the macula densa appeared faint. Cells of the proximal and distal convoluted tubules displayed pyknotic nuclei and vacuolated cytoplasm. The arterioles were engorged with blood, with extravasation of blood cells and infiltration by mononuclear cells (Figs. 1b, 1e, 1h).

The DM + Empagliflozin-treated group exhibited intact glomeruli. The parietal layer of Bowman's capsule consisted of simple squamous epithelium, while the visceral layer was formed of podocytes. Bowman's space was clearly delineated between the parietal layer and the glomeruli. The glomerular capillaries were lined with endothelial cells. Intraglomerular mesangial cells and matrix were observed between the capillary loops. Extraglomerular mesangial cells, macula densa, proximal and distal convoluted tubules, and arterioles appeared intact (Figs. 1c, 1f, 1i).

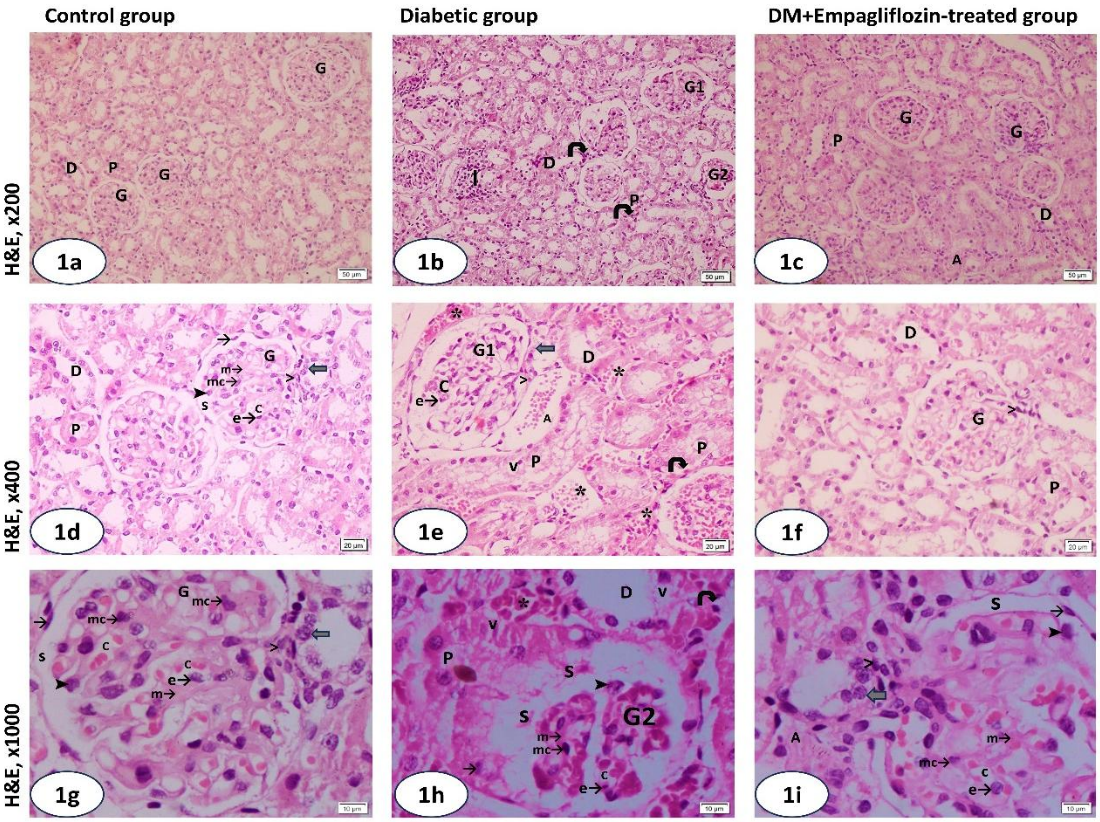

Fig. 1: Photomicrographs of renal cortical sections of the examined groups. **The control group [Figs. 1a, d, g]** shows renal corpuscles consisting of glomeruli (G) enclosed by Bowman's capsule. The parietal layer of Bowman's capsule is formed of simple squamous epithelium (thin arrow), and the visceral layer consists of podocytes (➤). Bowman's space (S) is clearly delineated between the parietal layer and the glomeruli. The glomerular capillaries (C) are lined with endothelial cells (e→). Intraglomerular mesangial cells (mc→) and matrix (m→), extraglomerular mesangial cells (>), and macula densa (thick arrow) are observed**.** The proximal convoluted tubules (P) have a narrow lumen and are lined by darkly stained cuboidal cells with rounded basally located nuclei and a prominent brush border. The distal convoluted tubules (D) are lighter with a wider lumen, centrally located nuclei, and lack a brush border. **The diabetic group [Figs. 1b, e, h]** shows a mixture of hypertrophied glomeruli (G1) and degenerated glomeruli (G2). The parietal layer of Bowman's capsule is thick and formed of cuboidal cells (thin arrow). Desquamated cells are observed in the dilated Bowman's space (S). The podocytes (➤) are scanty. Glomerular capillaries (C) are engorged with blood and lined with endothelial cells (e→) containing pyknotic nuclei. The intraglomerular mesangial cells (mc→) and matrix (m→) are intensely stained. The nuclei of the macula densa are faint (thick arrow). Cells of proximal (P) and distal (D) convoluted tubules show pyknotic nuclei (curved arrow) and vacuolated cytoplasm (V). Note the mononuclear cellular infiltration (I), engorged arteriole with blood (A), and extravasation of blood cells (asterisks). **The DM+Empagliflozin-treated group [Figs. 1c, f, i]** shows intact glomeruli (G). The parietal layer of Bowman's capsule consists of simple squamous epithelium (thin arrow), and the visceral layer is formed of podocytes (➤). Bowman's space (S) is clearly delineated between the parietal layer and the glomeruli. The glomerular capillaries (C) are lined with endothelial cells (e→). Intraglomerular mesangial cells (mc→) and matrix (m→) are observed between the capillary loops. Extraglomerular mesangial cells (>), macula densa (thick arrow), proximal (P) and distal (D) convoluted tubules, and arterioles (A) appear intact.
[H&E; Figs. 1a–c, ×200; Figs. 1d–f, ×400; Figs. 1g–i, ×1000, respectively]

1.2. PAS, Masson’s trichrome, and Sirius red Staining:

The PAS-stained control renal cortical sections showed weak positive PAS-staining of the glomerular capillary loops, mesangial matrix, tubular outlining, and arteriolar walls. Strong positive PAS-staining of the apical brush border of the proximal tubules was observed (Fig. 2a). The diabetic group showed strong positive PAS-staining of the glomerular capillary loops, mesangial matrix, tubular outlining, and arteriolar walls, and negative PAS-staining of the apical brush border of the proximal tubules (Fig. 2b). The DM+ Empagliflozin-treated group showed moderate positive PAS-staining of the glomerular capillary loops, mesangial matrix, tubular outlining, arteriolar walls, and apical brush border of the proximal tubules (Fig. 2c).

Masson’s trichrome-stained sections of the control renal cortex revealed minimal collagen fiber deposition within the renal corpuscles and intertubular regions (Fig. 2d). In contrast, the diabetic group exhibited intense collagen deposition in the renal corpuscles, arteriolar walls, and intertubular spaces (Fig. 2e). The DM+ Empagliflozin-treated group showed moderate collagen deposition in the renal corpuscles, arteriolar walls, and between the tubules (Fig. 2f).

Sirius red-stained sections of the control renal cortex demonstrated minimal collagen fiber deposition within the renal corpuscles and intertubular regions (Fig. 2g). The diabetic group exhibited intense collagen deposition in the renal corpuscles, arteriolar walls, and intertubular spaces (Fig. 2h). In the DM+Empagliflozin-treated group, moderate collagen deposition was observed in the renal corpuscles, arteriolar walls, and between the tubules (Fig. 2i).

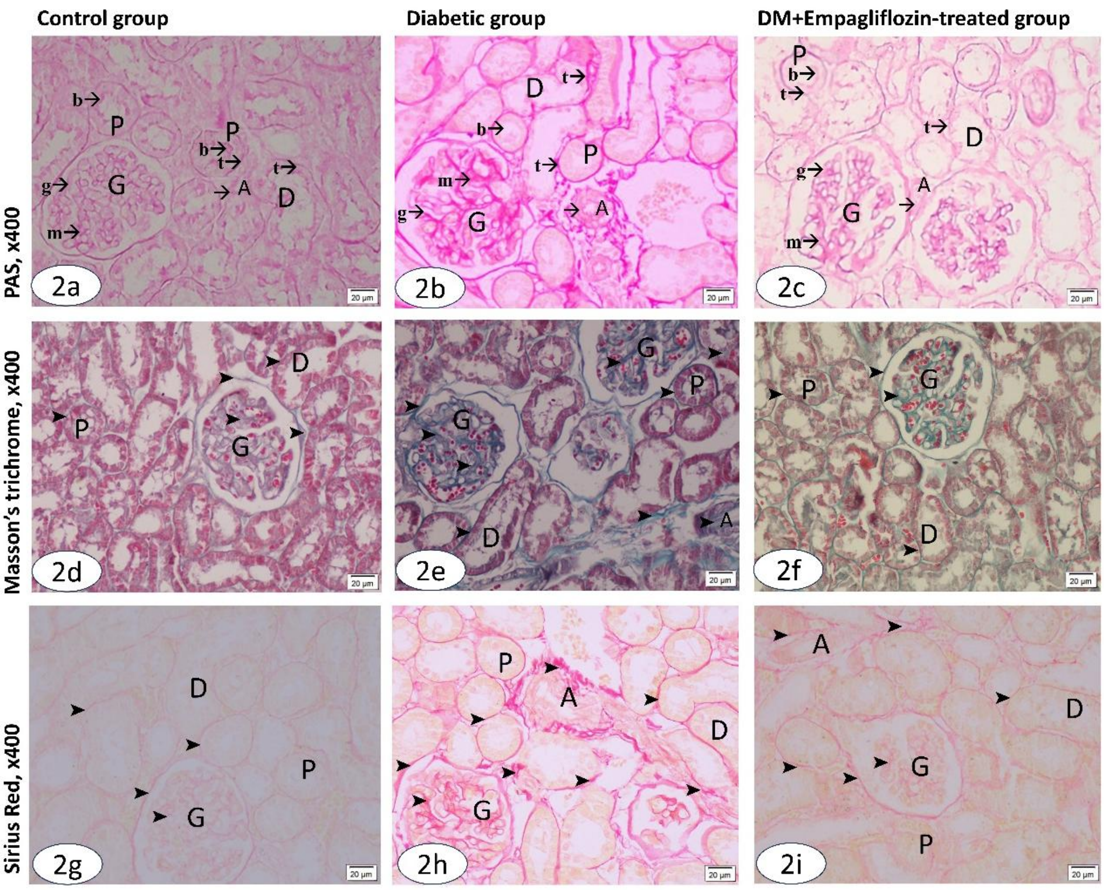

Fig. 2: Photomicrographs of PAS, Masson's trichrome, and Sirius red-stained renal cortical sections of the examined groups. **The control group** [**Figs. 2a, d, g**] shows weak positive PAS-staining of the glomerular capillary loops (g→), mesangial matrix (m→), tubular outlining (t→), and arteriolar walls (→). Strong positive PAS-staining of the apical brush border of the proximal tubules is observed (b→) [**Fig. 2a**]. Minimal collagen fiber deposition in the renal corpuscles and between the renal tubules (➤) in Masson's trichrome-stained sections [**Fig. 2d**] and Sirius red-stained sections **[Fig. 2g]** is observed**. The diabetic group** [**Figs. 2b, e, h]** shows strong positive PAS-staining of the glomerular capillary loops (g→), mesangial matrix (m→), tubular outlining (t→), and arteriolar walls (→) and negative PAS-staining of the apical brush border of the proximal tubules (b→) [**Fig. 2b**]. Intense collagen fiber deposition (➤) in the renal corpuscles, arteriolar walls, and between the tubules in Masson's trichrome-stained sections [**Fig. 2e**] and Sirius red-stained sections [**Fig. 2h**] is observed**. The DM+Empagliflozin-treated group** [**Figs. 2c, f, i**] shows moderate positive PAS-staining of the glomerular capillary loops (g→), mesangial matrix (m→), tubular outlining (t→), arteriolar walls (→), and apical brush border of the proximal tubules (b→) [**Fig. 2c**], moderate collagen fiber deposition (➤) in the renal corpuscles, arteriolar walls, and between the tubules in Masson's trichrome-stained sections [**Fig. 2f**] and Sirius red-stained sections [**Fig. 2i**]**.**

[PAS staining, Figs. 2a-c; Masson's trichrome staining, Figs. 2d–f; Sirius red staining, Figs. 2g–I, respectively; ×400. G, glomeruli; P, proximal convoluted tubules; D, distal convoluted tubules; A, arterioles]

1.3. Toluidine Blue Staining:

Toluidine blue-stained semithin sections of the control renal cortex demonstrated normal glomeruli and Bowman's spaces. The parietal layer of Bowman's capsule was lined with simple squamous epithelium, while the visceral layer consisted of podocytes. Glomerular capillaries were lined by endothelial cells. Intraglomerular mesangial cells and mesangial matrix were clearly identified. The proximal convoluted tubules were lined by cuboidal cells with rounded vesicular basal nuclei, displaying distinct apical brush borders and basal striations. The distal convoluted tubules exhibited a wider lumen and were lined by cuboidal cells with centrally located, rounded nuclei and pale cytoplasm (Figs. 3a, 3d, 3g).

The diabetic group exhibited hypertrophied glomeruli alongside others that appeared degenerated. The Bowman's space was dilated, often containing desquamated cells. The parietal layer of Bowman's capsule appeared thickened and was formed of cuboidal cells with large, rounded nuclei. Podocytes were scanty. The glomerular capillaries were sparse, and the intraglomerular mesangial cells were scanty and mesangial matrix showed degeneration. Cells of the proximal and distal convoluted tubules displayed pyknotic nuclei and vacuolated cytoplasm. Thick-walled arterioles, dilated interstitium, and mononuclear cellular infiltration were also observed (Figs. 3b, 3e, 3h).

The DM+Empagliflozin-treated group demonstrated intact glomeruli with clear Bowman's space. The parietal layer of Bowman's capsule was lined by simple squamous epithelium. The podocytes, glomerular capillaries with their endothelial lining, and intraglomerular mesangial cells and matrix were intact. The proximal convoluted tubules were lined by cuboidal cells with rounded vesicular nuclei and displayed well-preserved apical brush borders and basal striations. The distal convoluted tubules were lined by cuboidal cells with centrally located, rounded nuclei. Residual vacuolated cytoplasm, pyknotic nuclei, and thick-walled arterioles were also observed (Figs. 3c, 3f, 3i).

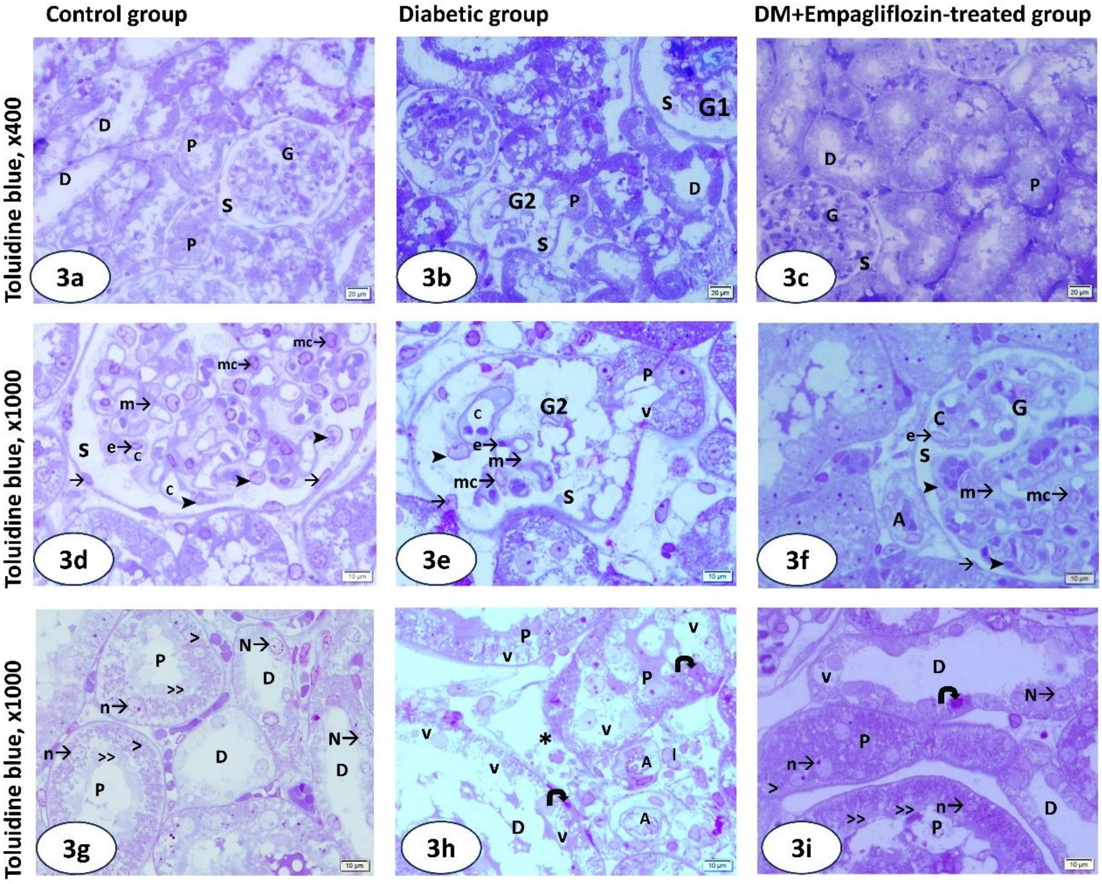

Fig. 3: Photomicrographs of Toluidine blue-stained renal cortical semithin sections of the examined groups. **The control group [Figs. 3a, d, g]** shows normal glomeruli (G), Bowman's space (S), simple squamous epithelium lining the parietal layer of Bowman's capsule (→), podocytes (➤), glomerular capillaries (C) with endothelial lining (e→), and intraglomerular mesangial cells (mc→) with matrix (m→). The proximal convoluted tubules (P) are lined by cuboidal cells with rounded vesicular basal nuclei (n→), exhibiting distinct apical brush borders (>>) and basal striations (>). The distal convoluted tubules (D) show a wider lumen and are lined by cuboidal cells with rounded central nuclei (N→) and pale cytoplasm. **The diabetic group** [**Figs. 3b, e, h]** shows hypertrophied glomeruli (G1), degenerated glomeruli (G2), and desquamated cells in the dilated Bowman's space (S). The parietal layer of Bowman's capsule is thickened and composed of cuboidal cells with large, rounded nuclei (→). Podocytes (➤) are scanty. Glomerular capillaries (C) are sparse. The nucleus of a glomerular endothelial cell (e→) is pyknotic. Intraglomerular mesangial cells (mc→) are scanty and mesangial matrix (m→) is degenerated. The proximal (P) and distal (D) convoluted tubules exhibit pyknotic nuclei (curved arrow) and vacuolated cytoplasm (V). Thick-walled arterioles (A), dilated interstitium (asterisks), and mononuclear cellular infiltration (I) are also noted. **The DM+Empagliflozin-treated group** [**Figs. 3c, f, i]** shows intact glomeruli (G), clear Bowman's space (s), the parietal layer of Bowman's capsule lined by simple squamous epithelium (→), podocytes (➤), glomerular capillaries (C) with endothelial lining (e→), intraglomerular mesangial cells (mc→), and mesangial matrix (m→). The proximal convoluted tubules (P) are lined by cuboidal cells with rounded vesicular nuclei (n→) and preserved apical brush borders (>>) and basal striations (>). The distal convoluted tubules (D) are lined by cuboidal cells with centrally located, rounded nuclei (N→). Residual vacuolated cytoplasm (V), pyknotic nuclei (curved arrow), and thick-walled arterioles (A) are observed.

[Toluidine blue; Figs. 3a–c, ×400; Figs. 3d–i, ×1000, respectively]

2. Electron Microscopic Results:

2.1. Scanning Electron Microscopic Results:

A scanning electron microscopic view of the control renal cortex revealed rounded glomeruli with tightly packed glomerular capillaries surrounded by Bowman's space, located between the smooth parietal layer and the glomerulus. At the vascular pole, two arterioles were observed with regular outer contours. Other arterioles exhibited a smooth, continuous endothelial lining and a well-defined circular lumen. Podocytes with large, flattened cell bodies, bulging nuclei, and long primary processes were observed. Each primary process gave rise to numerous secondary foot processes (pedicels), which interdigitated with those of adjacent podocytes and were separated by uniformly wide filtration slits. The proximal convoluted tubules exhibited thick walls and a narrow lumen, while the distal convoluted tubules appeared with thinner walls and a wider lumen (Figs. 4a, 4d, 4g).

The diabetic group showed degenerated, eroded glomeruli, widely separated capillary tufts, and dilated Bowman's space. The parietal layer had an interrupted outline. The podocytes revealed abnormally indented surfaces and shrunken nuclei. Irregular pedicels' interdigitation, primary processes lacking pedicels, fused pedicels, and abnormal widening of the filtration slits were observed. The proximal and distal convoluted tubules were eroded (Figs. 4b, 4e, 4h).

The DM+Empagliflozin-treated group displayed rounded glomeruli with well-formed loops of glomerular capillaries, clearly delineated Bowman's space, and a regular parietal layer. Podocytes showed large, flattened cell bodies with bulging nuclei and long primary processes, each giving rise to numerous pedicels. The proximal convoluted tubules exhibited thick cuboidal walls. Residual fused pedicels, widely separated capillary tufts, and widened filtration slits were also observed (Figs. 4c, 4f, 4i).

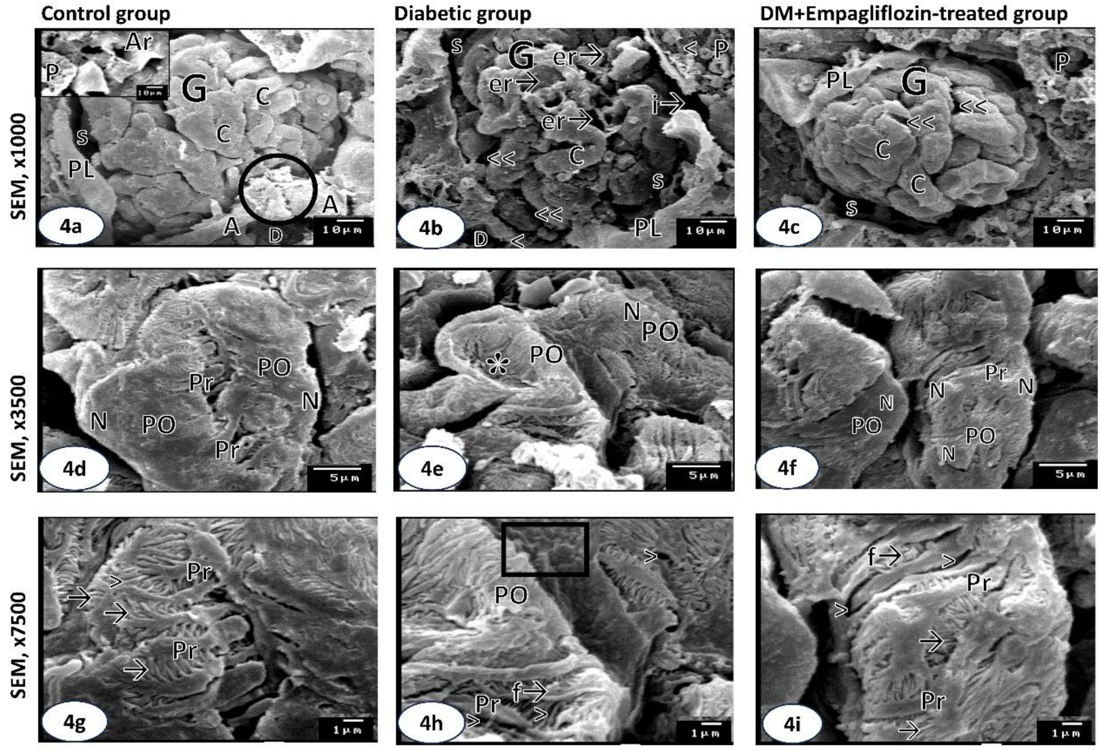

Fig. 4: Scanning electron microscopic photomicrographs of the renal cortex in the examined groups. **The control group [Figs. 4a, d, g]** shows rounded glomeruli (G). The glomerular capillaries (C) appear as tightly packed loops, while Bowman's space (S) is distinctly delineated between the smooth parietal layer (PL) and the glomerulus. At the vascular pole (circle), two arterioles (A) are observed with regular outer contours. The arteriole (Ar) shows smooth, continuous endothelial lining and a well-defined circular lumen. The proximal convoluted tubules (P) display thick walls and a narrow lumen. The distal convoluted tubules (D) exhibit thinner walls and wider lumina **[Fig. 4a, inset]**. Podocytes (PO) with large, flattened cell bodies, bulging nuclei (N), and long primary processes (Pr) **[Fig. 4d]**. Each primary process (Pr) gives rise to numerous pedicels (→), which interdigitate with those of neighboring processes and are separated by uniformly wide filtration slits (>) **[Fig. 4g]**. **The diabetic group [Figs. 4b, e, h]** exhibits degenerated glomeruli (G), glomerular erosion (er→), and dilated Bowman's space (S). The capillary tufts (C) are separated by wide spaces (<<). The parietal layer (PL) displays an interrupted outline (i→). Both proximal (P) and distal (D) convoluted tubules show erosion (<) **[Fig. 4b]**. Podocytes (PO) demonstrate abnormally indented surfaces (asterisk) and shrunken nuclei (N) **[Fig. 4e]**. Irregular interdigitation of the pedicels (rectangle), a primary process lacking pedicels (Pr), fused pedicels (f→), and widened filtration slits (>) are observed **[Fig. 4h]**. **The DM+Empagliflozin-treated group [Figs. 4c, f, i]** displays rounded glomeruli (G) with well-formed loops of capillaries (C), clearly delineated Bowman's space (S), and a regular parietal layer (PL). The proximal convoluted tubules (P) exhibit thick cuboidal walls. Residual widened spaces between capillary tufts (<<) are noted **[Fig. 4c]**. Podocytes (PO) show large, flattened cell bodies with bulging nuclei (N) and long primary processes (Pr), each giving rise to numerous pedicels (→). Residual fused pedicels (f→) and widened filtration slits (>) are also observed **[Figs. 4f, i]**.

[SEM; Figs. 4a–c and inset, ×1000; Figs. 4d–f, ×3500; Figs. 4g–i, ×7500, respectively]

2.2. Transmission Electron Microscopic Results:

Transmission electron microscopic examination of the renal cortical ultrathin sections of the control group revealed podocytes with folded nuclei, prominent nucleoli, primary processes, and pedicels separated by filtration slits of uniform width. The glomerular capillaries were seen with a uniform basement membrane formed of lamina densa, bordered by lamina rara externa and lamina rara interna. Bowman’s space and regular fenestrations of the capillary endothelial cell lining were observed (Figs. 5a, 5d). The proximal convoluted tubular cells had euchromatic basal nuclei, apical microvilli projecting into the lumen, and numerous elongated mitochondria located within cytoplasmic compartments formed by deep basal infoldings of the intact plasma membrane (Fig. 5g). The distal convoluted tubular cells had euchromatic central nuclei, rough endoplasmic reticulum, ribosomes, mitochondria, and regular plasma membranes (Fig. 5j).

The diabetic group showed thickening of the glomerular basement membrane. The lamina densa was bordered by a distorted lamina rara interna. The glomerular endothelial cells revealed irregular fenestrations. The podocytes had shrunken nuclei and abnormally fused pedicels. Wide filtration slits and electron-dense mesangial matrix were observed (Figs. 5b, 5e). The proximal convoluted tubular cells exhibited small, darkly stained nuclei, mitochondria with destructed cisternae, rarefied cytoplasm, a wide lumen, and a thickened plasma membrane. The apical surface exhibited degenerated microvilli projecting into a widened lumen with focal areas of microvillar loss (Fig. 5h). The distal convoluted tubular cells had condensed, disfigured nuclei, a thickened basal plasma membrane, and a wide lumen. The cytoplasm revealed electron-dense mitochondria and cytoplasmic rarefaction (Fig. 5k).

The DM+Empagliflozin-treated group showed an intact glomerular basement membrane, lamina densa, lamina rara interna, lamina rara externa, endothelial fenestrations, podocytes, and pedicels. Residual fused pedicels and wide filtration slits were seen (Figs. 5c, 5f). The proximal convoluted tubular cells had rounded nuclei, elongated mitochondria located within cytoplasmic compartments formed by deep basal infoldings, and apical microvilli projecting into the lumen. The plasma membrane retained its normal thickness. Residual cytoplasmic rarefaction was observed (Fig. 5i). The distal convoluted tubular cells had central euchromatic nuclei, mitochondria, ribosomes, and an intact basement membrane. Residual cytoplasmic rarefication was seen (Fig. 5I).

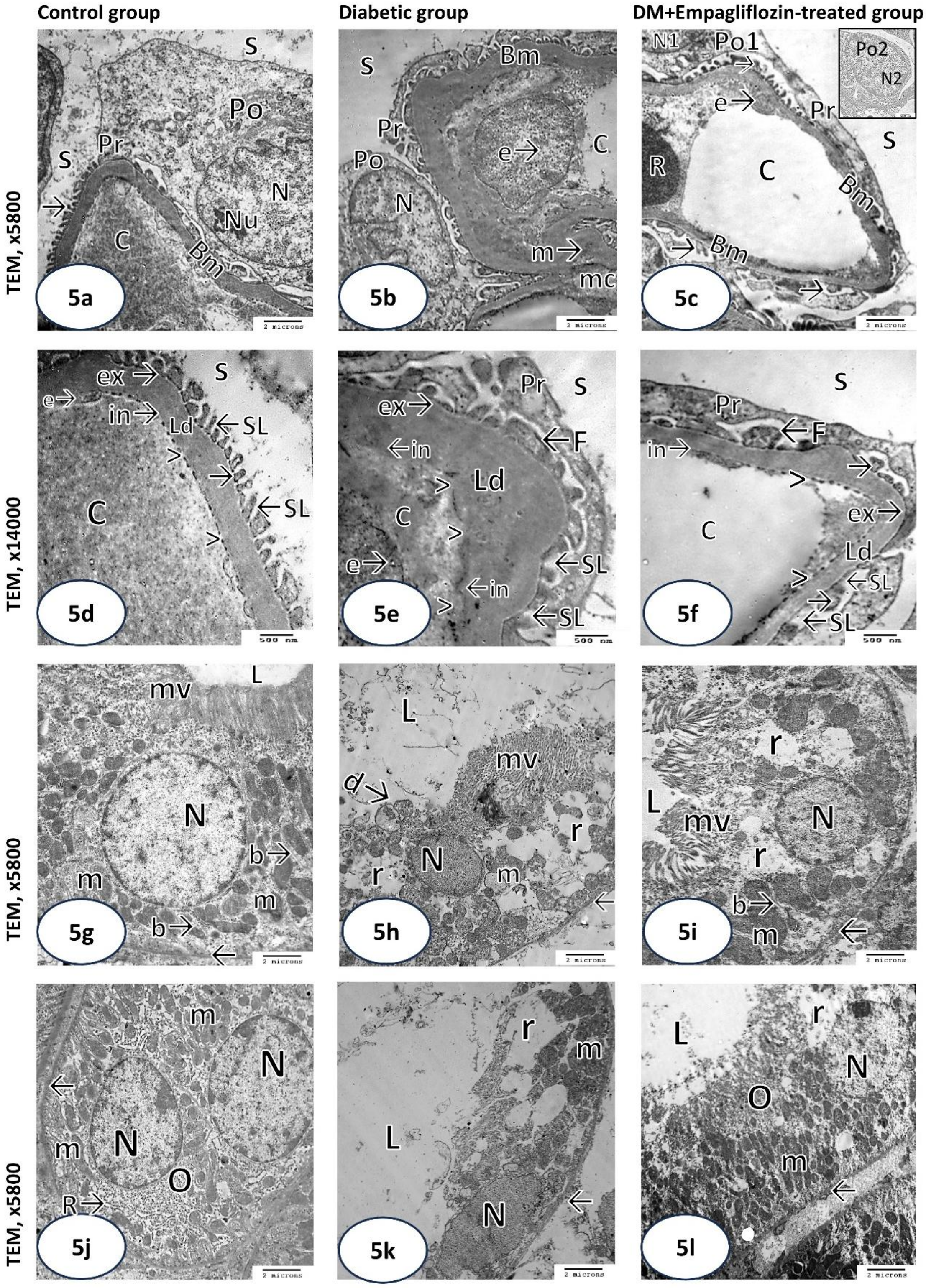

Fig. 5: Transmission electron microscopic photomicrographs of the renal cortical ultrathin sections of the examined groups. **The control group** [**Figs. 5a, d, g, j**] reveals Bowman's space (S), a podocyte (Po) with a folded nucleus (N), a prominent nucleolus (Nu), a primary process (Pr), and pedicels (→) separated by filtration slits (←SL). The glomerular capillaries (C) are seen with a uniform basement membrane (Bm) formed of lamina densa (Ld) bordered by lamina rara externa (ex→) and lamina rara interna (in→). Note the regular fenestrations (>) within the endothelial cells lining the capillaries (e→) [**Figs. 5a, d**]. The proximal convoluted tubular cells have euchromatic basal nuclei (N), apical microvilli (mv) projecting into the lumen (L), and elongated mitochondria (m) located within cytoplasmic compartments formed by deep basal infoldings (b→) of the intact plasma membrane (←) **[Fig. 5g].** Two adjacent distal convoluted tubular cells

reveal euchromatic central nuclei (N), rough endoplasmic reticulum (R→), ribosomes (O), mitochondria (m), and regular plasma membrane (←) **[Fig. 5j]. The diabetic group** [**Figs. 5b, e, h, k]** shows thickening of the glomerular basement membrane (Bm). The lamina densa (Ld) is bordered by a distorted lamina rara interna (←in). The endothelial fenestrations (>) are irregular. The podocytes (Po) have shrunken nuclei (N) and abnormally fused pedicels (F→). Wide filtration slits (←SL) and electron-dense mesangial matrix (m→) are observed. Note the Bowman's space (S), lamina rara externa (ex→), primary podocyte processes (Pr), glomerular capillaries (C), endothelial cell lining (e→), and mesangial cells (mc) [**Figs. 5b, e].** The proximal convoluted tubular cells reveal small, darkly stained nuclei (N), mitochondria with destructed cisternae (m), rarefied cytoplasm (r), and a thickened basal plasma membrane (←). The apical surface exhibits degenerated microvilli (mv) projecting into a widened lumen (L), with focal areas of microvillar loss (d→) **[Fig. 5h].** The distal convoluted tubular cells have condensed, disfigured nuclei (N), a thickened basal plasma membrane (←), and a wide lumen (L). The cytoplasm reveals electron-dense mitochondria (m) and rarefaction (r) [**Fig. 5k]. The DM+Empagliflozin-treated group** [**Figs. 5c, f, i, I]** shows an intact glomerular basement membrane (Bm) and pedicels (→). Note the podocyte (Po1) with a nucleus (N1) and a primary process (Pr), Bowman's space (S), glomerular capillary lumen (C), endothelial lining (e→**)** and red blood cells (R). An intact podocyte (Po2) with a nucleus (N2) is shown **[Fig. 5c, inset].** Intact primary process (Pr), lamina densa (Ld), lamina rara interna (in→), lamina rara externa (ex→), Bowman's space (S), glomerular capillary lumen (C), pedicels (→), and endothelial fenestrations (>). Residual fused pedicels (←F) and wide filtration slits (←SL) are observed [**Fig. 5f].** The proximal convoluted tubular cells have rounded nuclei (N), elongated mitochondria (m), basal infoldings (→), and apical microvilli (mv) projecting into the lumen (L), and intact plasma membrane (←). Residual cytoplasmic rarefaction (r) is observed **[Fig. 5i].** The distal convoluted tubular cells have central euchromatic nuclei (N), mitochondria (m), ribosomes (O), and an intact plasma membrane (←). Residual cytoplasmic rarefication (r) is seen. Note the lumen (L) **[Fig. 5l].**

[TEM; Figs. 5a–c and inset, ×5800; Figs. 5d–f, ×14,000; Figs. 5g–l, ×5800, respectively]

IV- Immunohistochemical Results:

There were no obvious differences in the immunohistochemical findings between the control and sham groups throughout the experiment. Therefore, only photomicrographs of the immunohistochemical expression of the control group were included. The control group revealed weak positive caspase-3 immunoreactivity (Fig. 6a), along with strong positive connexin-43 immunoreactivity (Fig. 6d) and Nrf2 immunoreactivity (Fig. 6g) within the glomeruli and tubules. In contrast, the diabetic group exhibited strong positive caspase-3 immunoreactivity (Fig. 6b), while connexin-43 immunoreactivity (Fig. 6e) and Nrf2 (Fig. 6h) immunoreactivity were weakly positive in the same structures. The diabetic group treated with empagliflozin showed moderate positive immunoreactivity for caspase-3 (Fig. 6c), connexin-43 (Fig. 6f), and Nrf2 (Fig. 6i) within the glomeruli and tubules.

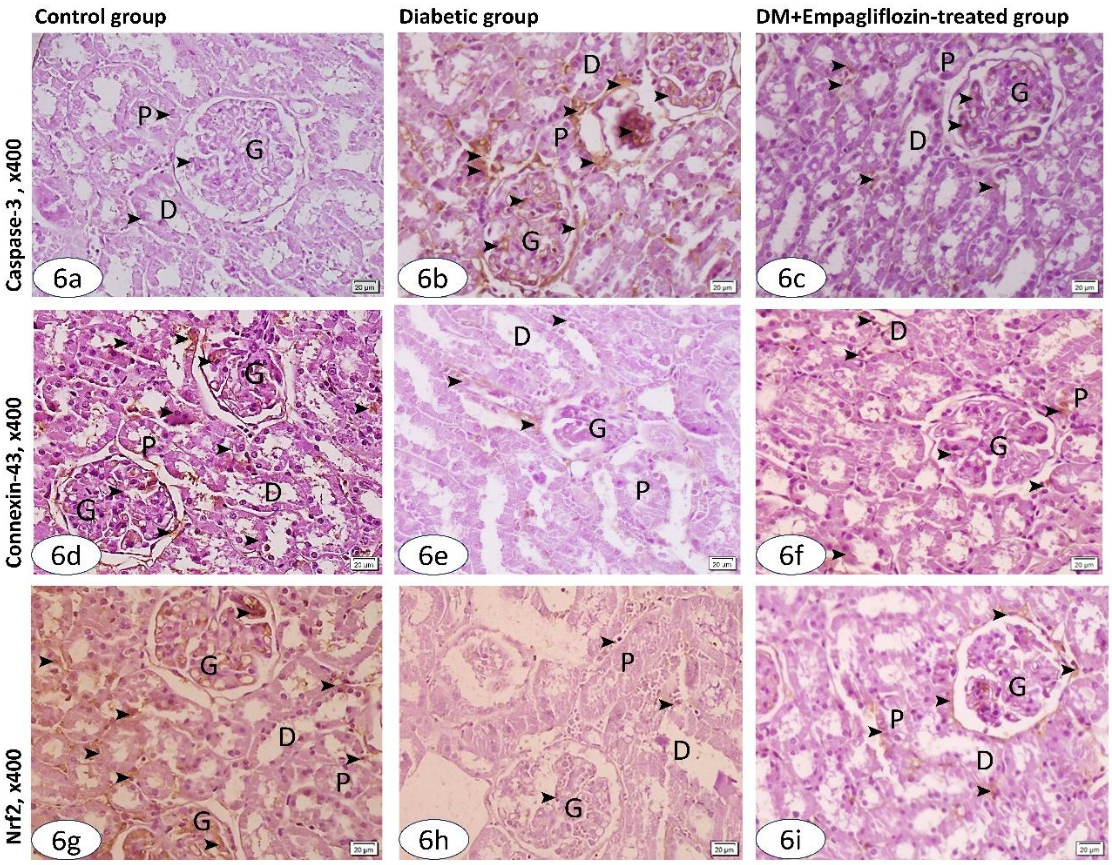

Fig. 6: Photomicrographs of the immunohistochemical expression of caspase-3, connexin-43, and Nrf2 in the renal cortex of the examined groups. **The control group** [**Figs. 6a, d, g]** shows weak positive caspase-3 immunoreactivity (➤) **[Fig. 6a]**, along with strong positive connexin-43 immunoreactivity (➤) **[Fig. 6d]** and Nrf2 immunoreactivity (➤) **[Fig. 6g]** localized within the glomeruli and proximal and distal tubules. **The diabetic group** [**Figs. 6b, e, h]** demonstrates strong positive caspase-3 immunoreactivity (➤) **[Fig. 6b]**, accompanied by weak positive connexin-43 immunoreactivity (➤) **[Fig. 6e]** and Nrf2 immunoreactivity (➤) **[Fig. 6h]** in the same structures. **The DM+Empagliflozin-treated group** [**Figs. 6c, f, i]** exhibits moderate positive caspase-3 immunoreactivity (➤) [**Fig. 6c]**, connexin-43 immunoreactivity (➤) [**Fig. 6f]**, and Nrf2 immunoreactivity (➤) [**Fig. 6i]** within the glomeruli and tubules.
[Immunohistochemical staining for caspase-3, Figs. 6a–c; connexin-43, Figs. 6d–f; Nrf2, Figs. 6g–l, respectively; ×400. G, glomeruli; P, proximal convoluted tubules; D, distal convoluted tubules]

DISCUSSION

Diabetes mellitus (DM) represents a major global health challenge, with its prevalence continuing to rise worldwide (Fayed *et al.,* 2025). Accumulating evidence demonstrates that individuals with DM are at a substantially higher risk of developing nephropathy compared to non-diabetic individuals (Ahmed *et al.,* 2023). Given the high incidence and serious complications associated with DM, further researches into the disease and the optimization of therapeutic strategies to reduce the burden of diabetes-related complications remain essential (Fioretto & Mauer, 2007).

The marked hyperglycemia observed in the present study following alloxan administration confirms the successful induction of diabetes mellitus. This finding aligns with the study of Amer *et al.* (2022), which demonstrated alloxan's selective cytotoxicity on pancreatic β-cells.

The significant reduction in hyperglycemia observed with empagliflozin treatment in the present study is consistent with its well-established glucose- lowering mechanism , which involves inhibition of the sodium-glucose cotransporter-2 (SGLT2) in the proximal tubules, thereby enhancing urinary glucose excretion, as reported by Kräker *et al.* (2020). A similar finding was demonstrated by Alqudah *et al.* (2024), who showed that empagliflozin administration to STZ-induced diabetic rats resulted in a marked reduction in glycated hemoglobin (HbA1c) levels.

In the present study, the diabetic group exhibited distinct glomerular alterations, including hypertrophy in some glomeruli, while others appeared degenerated. Additional changes included marked thickening of the glomerular basement membrane. These findings are consistent with the observations of Fu *et al.* (2022), who reported basement membrane thickening in mice following seven months of streptozotocin (STZ)-induced diabetes. Similarly, Hsu *et al.* (2024) described diabetic nephropathy as being characterized by extensive remodeling of the glomerular architecture. Williams *et al.* (2022) linked hyperglycemia to the structural alterations in the renal cortex, particularly within the glomeruli.

At the molecular level, Fung *et al.* (2025) revealed that hyperglycemia stimulated reactive oxygen species (ROS) production and activated protein kinase C and nuclear factor kappa B (NF-κB), thereby promoting the formation of advanced glycation end-products, lipotoxicity, and oxidative stress. They further noted that hyperglycemia triggered abnormal intracellular signaling, contributing to glomerular destruction.

The present work revealed irregular endothelial fenestrations in the diabetic group. In agreement, Rayego-Mateos *et al.* (2020) and Yang and Liu (2022) emphasized that endothelial cell injury represented one of the earliest pathological events in diabetic nephropathy. Moreover, Liu *et al.* (2022a and 2022b) demonstrated that significant glomerular damage preceded the onset of microalbuminuria in diabetic patients.

The present study exhibited scanty podocytes with degenerative features, abnormal pedicels' interdigitation, and widening of the filtration slits in the diabetic animals. Reports by Li *et al.* (2023) and Gil *et al.* (2020) highlighted the pivotal role of podocytes in maintaining the glomerular filtration barrier, with their injury leading to proteinuria.

Furthermore, the diabetic group of the current study exhibited tubular degeneration, cytoplasmic vacuolization, loss of the proximal tubular brush border, and thickening of the tubular basement membranes. Comparable findings were described in the review of Fioretto and Mauer (2007) and observed by Lin *et al.* (2018), as well as Yang *et al.* (2024), following intraperitoneal STZ administration in mice. Forbes and Cooper (2013) highlighted that diabetes is associated with impaired mitochondrial function and dysregulation of key signaling cascades, including the polyol pathway, thereby further exacerbating renal tissue damage.

Glomerular and tubular structural improvements were observed with empagliflozin treatment in the present study. Comparable results were reported by Williams *et al.* (2022) in the setting of diabetes complicated by hypertension. They established hypertensive diabetic rat models using streptozotocin-induced type 1 diabetic Dahl salt-sensitive (STZ-SS) rats and deoxycorticosterone-salt hypertensive type 2 diabetic nephropathy (T2DN) rats. Their findings demonstrated that empagliflozin effectively controlled blood glucose levels and attenuated the progression of renal fibrosis in both hypertensive type 1 and type 2 diabetic rats, particularly when combined with lisinopril for blood pressure control. In addition, Palmar and Clegg (2023) demonstrated that SGLT2 inhibitors, by mimicking a fasting-like state, could activate molecular pathways that support optimal cellular function. Furthermore, Iordan *et al.* (2024) showed that SGLT2 inhibition in kidney disease reduced renal oxygen consumption and downregulated hypoxia-inducible factor 1-alpha (HIF-1α), a key mediator of kidney injury. They further noted that SGLT2 inhibitors decreased kidney injury molecule-1 (KIM-1) level, a sensitive marker of tubular damage.

Moreover, the diabetic group in the present study demonstrated thickening of the arteriolar walls. This finding is consistent with the document of Rask-Madsen and King (2013), who emphasized that vascular complications represented the most serious manifestations of diabetes. Similarly, Ahmed *et al.* (2023) reported that arteriolar thickening occurred in both afferent and efferent vessels of diabetic subjects, with the efferent arterioles being more severely affected. They further noted that this progressive alteration could contribute to hypertension and ischemic nephropathy.

Empagliflozin treatment in the present study, ameliorated this effect. Similarly, Neutel *et al.* (2023) observed that empagliflozin reduced arterial stiffness in aged mice. They reported that empagliflozin reduced the ageing-associated increase in collagen type I in the medial layer of the abdominal infrarenal aorta and decreased medial TGF-β deposition.

In addition, the diabetic group in the present study exhibited inflammatory cell infiltration, a finding that aligns with the report of Lin *et al.* (2024), who described inflammation as a hallmark of diabetic nephropathy. According to their study, elevated levels of cytokines and chemokines promote fibrosis and increase vascular permeability, thereby exacerbating renal injury.

The present study demonstrated that empagliflozin ameliorated diabetes-induced renal cortical inflammation. This effect may be explained by the ability of empagliflozin to attenuate C4d overactivation, thereby reducing complement-mediated injury and suppressing chronic inflammatory signaling, as reported by Fayed *et al.* (2025).

In the present study, the strong positive PAS staining of the glomerular basement membrane corresponded with its observed thickening. The negative PAS staining of the proximal tubular brush borders was consistent with the previously noted loss of brush border integrity. These findings further confirm diabetes-induced damage to both the glomerular filtration barrier and the tubular epithelium, and they align with the observations of Yuan *et al.* (2017), who highlighted that PAS staining could reveal the enhanced accumulation of advanced glycation end-products in the renal cortex of diabetic rats, supporting its utility as a marker of diabetes-related histopathological changes.

Empagliflozin treatment normalized the renal cortical PAS staining of the diabetic group of the present work. This effect might be attributed to the fasting-like state induced by SGLT2 inhibitors, which activates molecular pathways that support optimal cellular function, as reported by Palmar and Clegg (2023) and previously mentioned.

The present work demonstrated marked collagen deposition and interstitial fibrosis in the diabetic renal sections stained by Masson’s trichrome and Sirius red. These findings are consistent with the studies of Yuan *et al.* (2017) and Fung *et al.* (2025), who observed thickened collagen fibers within the glomerular basement membrane, mesangium, and interstitium of diabetic animals. According to Hsu *et al.* (2024), such fibrotic changes are hallmark features of diabetic kidney disease, and they progressively compromise renal structure and function.

The present study revealed that empagliflozin mitigated the renal cortical fibrosis. Similarly, Huang *et al.* (2024) reported that empagliflozin attenuated renal interstitial fibrosis in diabetic kidney disease by inhibiting lymphangiogenesis and lymphatic endothelial-to-mesenchymal transition through the VEGF-C/VEGFR3 signaling pathway.

In the diabetic renal cortex of the present study, the strong positive caspase-3 immunoreaction reflects enhanced apoptosis within renal cortical tissue. A similar finding was observed by Ahmed *et al.* (2022) in some epithelial tumors. They stated that positive caspase-3 staining directly indicated the presence of active cells undergoing apoptosis, thereby aggravating structural deterioration.

In the present work, empagliflozin treatment reduced caspase-3 expression in diabetic rats, indicating decreased apoptosis. This finding is consistent with the results of Iordan *et al.* (2024), who reported that SGLT2 inhibitors decreased kidney injury molecule-1 (KIM-1) level as mentioned before.

Concurrently, the weak connexin-43 expression within the renal cortical tissue of diabetic rats in the present study indicates disrupted gap junction communication and altered intercellular signaling, consistent with the findings of Roger *et al.* (2022), who reported that in a diabetic mouse model, decreased connexin-43 expression was associated with the development and progression of diabetic retinopathy. In contrast, Genest *et al.* (2024) demonstrated that endothelial-specific deletion of connexin-43 improved renal function and structure following acute kidney injury. This underscores the controversy that the effects of connexin-43 deletion or modulation are cell type-dependent, since tubular epithelial connexin-43 deletion in the same study did not confer similar protection.

The empagliflozin-treated diabetic group of the present study revealed an improvement in connexin-43 expression. Similar findings were reported by El-Shafei *et al.* (2023), who demonstrated that empagliflozin in combination with platelet-rich plasma significantly ameliorated cisplatin-induced cardiac damage in rats by alleviating oxidative stress, suppressing inflammation, and inhibiting apoptosis.

The weak Nrf2 immunoreaction observed in the diabetic renal cortex in the present study suggests impaired activation of the antioxidant defense pathway, thereby rendering tissues more susceptible to oxidative stress-mediated damage as mentioned by Montes *et al.* (2015), who examined Nrf2-antioxidant response element activity as an indicator of cadmium-induced oxidative stress in developing rats, and Barakat *et al.* (2022) in the context of developing non-melanoma skin cancer.

In the current work, empagliflozin treatment upregulated Nrf2 expression, indicating activation of antioxidant defense pathways. This observation is in line with Badreldin *et al.* (2024), who demonstrated that empagliflozin-mediated targeting of the Nrf2/HO-1 and NF-κB/TNF-α signaling pathways protected against atrial fibrillation-induced acute kidney injury in rats.

Collectively, the immunoreactive alterations observed in the diabetic group, and their amelioration following empagliflozin treatment, were consistent with the histological and morphometric findings of the present study.

Conclusion

This study demonstrated the beneficial effects of empagliflozin in mitigating structural and ultrastructural renal cortical damage associated with alloxan-induced diabetes through its anti-fibrotic and anti-apoptotic actions, enhancement of intercellular communication, and upregulation of antioxidant enzyme expression, indicating that empagliflozin could be valuable in the management of such a disease.

Declarations:

Ethics Approval: This research protocol was approved by the Institutional Review Board of the Faculty of Medicine, Assiut University (Approval No.: 04-2025-300652).

Compliance with Ethical Statements: All applicable guidelines for the care and use of animals were followed.

Competing Interests: The authors declare that there is no conflict of interest.

Author contribution: Reneah Refaat Bushra designed the research, acquired the data, recorded the measurements, analyzed the data, wrote the manuscript, and discussed the results.

Data Availability Statement: Data supporting the findings of this study are available from the corresponding author upon reasonable request.

Funding Information: This research did not receive any funding from any agencies.

Acknowledgment: Not applicable.

REFERENCE

Ahmed G.; Abdelaziz H.; El Sayed H. and Adly M. (2023). Histopathological changes on the kidney and lung of experimentally induced diabetic rats. South Valley University-International Journal of Medical Sciences; 6(1): 594-601. DOI: 10.21608/SVUIJM.2020.47895.1020

Ahmed S.; Bernaba C. and Muhammad E. (2022). Immunohistochemical expression of caspase-3 in some epithelial tumors. South Valley University-International Journal of Medical Sciences; 5(1): 37-45. DOI: 10.21608/svuijm.2022.212147

Alqudah S.; Hailat M.; Zakaraya Z.; Abu Dayah A.; Abu Assab M.; Alarman S.; et al. (2024). Impact of Opuntia ficus-indica juice and empagliflozin on glycemic control in rats. Current Issues in Molecular Biology; 46(11): 12343-12353. DOI: 10.3390/cimb46110733

Amer A.; Mohamed R.; Bastwrous A. and Adly M. (2022). Maternal alloxan exposure induces damage in rat offspring lumbar vertebrae and the protective role of arachidonic acid. Romanian Journal of Morphology and Embryology; 63(1): 83-97. DOI:10.47162/RJME.63.1.08

Badreldin H.; El-Karef A.; Ibrahim T. and Elshal M. (2024). Targeting Nrf2/HO-1 and NF-κB/TNF-α signaling pathways with empagliflozin protects against atrial fibrillation-induced acute kidney injury in rats. Toxicology; 506: 153879. DOI: 10.1016/j.tox.2024.153879

Barakat A.; El-Sharkawy S. and El-Din S. (2022). Immunohistochemical expression of the nuclear factor-erythroid-2-related factor 2 (NRF2) in nonmelanoma skin cancer. Menoufia Medical Journal; 35(3): 927-934. DOI: 10.4103/mmj.mmj_37_22

Chew D. and Schenck P. (2023). Renal anatomy, physiology, and evaluation of function. In: Urinalysis in the Dog and Cat. John Wiley & Sons; pp. 1-36. DOI: 10.1002/9781119380443

Colbert G.; Madariaga H.; Gaddy A.; Elrggal M. and Lerma E. (2023). Empagliflozin in adults with chronic kidney disease (CKD): Current evidence and place in therapy. Therapeutics and Clinical Risk Management; 19:133–142. DOI: 10.2147/TCRM.S398163

El-Shafei A.; Hassan R. and Hosny S. (2023). A comparative histological and immune-histochemical study on the possible therapeutic effects of empagliflozin and platelet-rich plasma against cisplatin-induced cardiotoxicity in rats. Egyptian Journal of Histology; 46(1): 378-493. DOI: 10.21608/ejh.2021.69267.1451

Fayed A.; Fathy A.; Rakha N.; Soliman K. and Hammad H. (2025). The effect of empagliflozin on alleviating C4d over-activation in diabetic kidney disease, The American Journal of the Medical

Sciences; 369(5): 568-573. DOI: 10.1016/j.amjms.02.002

Fioretto P. and Mauer M. (2007): Histopathology of diabetic nephropathy. Seminars in Nephrology; 27(2): 195-207. DOI: 10.1016/j.semnephrol. 2007. 01.012

Forbes J. and Cooper M. (2013). Mechanisms of diabetic complications. Physiological Reviews; 93(1): 137-188. DOI: 10.1152/physrev.00045.2011

Fu J.; Shinjo T.; Li Q.; St-Louis R.; Park K.; Yu M.; et al. (2022). Regeneration of glomerular metabolism and function by podocyte pyruvate kinase M2 in diabetic nephropathy. Journal of Clinical Investigation; 7(5): 1-19. DOI: 10.1172/jci.insight.155260

Fung A.; Li Z.; Boote C.; Markov P.; Gaut J.; Jain S.; et al. (2025). Label-free multimodal optical biopsy reveals biomolecular and morphological features of diabetic kidney tissue in 2D and 3D. Nature Communications; 16(1): 1-13. DOI: 10.1038/s 41467-025-59163-w

Gartner L. and Lee L. (2024). The urinary system. In: Board Review Series: Cell Biology and Histology (9th edition, Chapter 18, pp. 332-350). Wolters Kluwer Health. ISBN:9781975219741

Genest M.; Kinugasa S.; Roger E.; Boutin L.; Placier S.; Figueroa S.; et al. (2024). Endothelial-specific deletion of connexin 43 improves renal function and structure after acute kidney injury. Molecular Medicine; 30(1): 261-274. DOI: 10. 1186/s10020-024-01011-6

Gil C.; Hooker E. and Larrivée B. (2020). Diabetic kidney disease, endothelial damage, and podocyte-endothelial crosstalk. Kidney Medicine; 3(1):105–115. DOI: 0.1016/j.xkme.2020.10.005

Groyer H.; Supiot R.; Tardu J.; Virely N.; Sivignon M.; San D.; et al. (2024). Cost-effectiveness of empagliflozin (JARDIANCE®) in the treatment of patients with chronic kidney disease in France, based on the EMPA-KIDNEY clinical trial. Clinical Drug Investigation; 44(11):811-828. DOI: 10.1007/s40261-024-1398-4

Heikal S.; Mahmoud S.; El-Dosoky M. and Mohamed H. (2024). Isolation and identification of potassium-solubilizing bacteria from wheat rhizosphere (Triticum aestivum L.). Assiut Journal of Agricultural Sciences; 55 (4): 259-276. DOI: 10.21608/ AJAS.2024.298805.1373

Hsu Y.; Shih Y.; Ho C.; Liu C.; Liaw C.; Lin H.; et al. (2024). Ethyl acetate fractions of Salvia miltiorrhiza Bunge (Danshen) crude extract modulate fibrotic signals to ameliorate diabetic kidney injury. International Journal of Molecular Sciences; 25(16):1-18. DOI: 10.3390/ijms25168986

Huang J.; Liu Y.; Shi M.; Zhang X.; Zhong Y.; Guo S.; et al. (2024). Empagliflozin attenuates renal interstitial fibrosis in diabetic kidney disease by inhibiting lymphangiogenesis and lymphatic endothelial-to-mesenchymal transition via the VEGF-C/VEGFR3 pathway. Biomedicine & Pharmacotherapy ;180:1-18. DOI: 10.1016/j. biopha

Iordan L.; Gaita L.; Timar R.; Avram V.; Sturza A. and Timar B. (2024). The renoprotective mechanisms of sodium-glucose cotransporter-2 inhibitors (SGLT2i): A narrative review. International Journal of Molecular Sciences; 25(13):1–26. DOI: 10.3390/ ijms25137057

Jha R.; Lopez-Trevino S.; Kankanamalage H. and Jha J. (2024). Diabetes and renal complications: An overview on pathophysiology, biomarkers, and therapeutic interventions.

Biomedicines; 12(5):1–23. DOI: 10.3390/biomedicines12051098

Jovanovic I.; Ugrenovic S. and Jovanovic A. (2021). Use of ImageJ for measuring optical density. Journal of Multimedia Processing and Technologies; 12(2): 35-40. DOI: 10.6025/jmpt/ 2021/12/2/35-40

Kler C.; Mezger A. and Wild S. (2022). Comparative evaluation of free web tools ImageJ and Photopea for the surface area quantification of planar substrates and organisms. Diversity; 14(4): 272. DOI: 10. 3390/d14040272

Korkmaz S. and Demir Y. (2023). Investigation of some univariate normality tests in terms of type-I errors and test power; Journal of Scientific Report-A (52): 376-395. DOI: 10.59313/ jsr-a.1222979

Kräker K.; Herse F.; Golic M.; Haase N.; Verhaegh R.; Krüger K.; et al. (2020). Effects of empagliflozin and target-organ damage in a novel rodent model of heart failure induced by combined hypertension and diabetes. Scientific Reports; 10(1): 14061. DOI: 10.1038/s41598-020-70708-5

Kumar M.; Muthurayar T.; Karthika S.; Gayathri S.; Varalakshmi P. and Ashokkumar B. (2025). Anti-diabetic potentials of Lactobacillus strains by modulating gut microbiota structure and β-cell regeneration in the pancreatic islets of alloxan-induced diabetic rats. Probiotics and Antimicrobial Proteins; 17(3): 1096-1116. DOI: 10.1007/s 12602-024-10221-7

Li C.; Zhang J.; Xue M.; Li X.; Han F.; Liu X.; et al. (2019). SGLT2 inhibition with empagliflozin attenuates myocardial oxidative stress and fibrosis in diabetic mice hearts. Cardiovascular Diabetology;18(1):15. DOI: 10. 1186/s12933-019-0816-2

Li X.; Zhang Y.; Xing X.; Li M.; Liu Y.; Xu A.; et al. (2023). Podocyte injury of diabetic nephropathy: Novel mechanism discovery and therapeutic prospects. Biomedicine & Pharmacotherapy ;168:115670. DOI: 10.1016/j. biopha.115670

Lin D.; Yang T.; Ho C.; Shih Y.; Lin C. and Hsu Y. (2024). Targeting macrophages: Therapeutic approaches in diabetic kidney disease. International Journal of Molecular Sciences; 25(8): 1-29. DOI: 10.3390/ijms25084350

Lin Y.; Chang Y.; Yang S.; Wu K. and Chu T. (2018). Update of pathophysiology and management of diabetic kidney disease. Journal of the Formosan Medical Association; 117(8): 662-675. DOI: 10.1016/j. jfma. 2018.02.007

Liu H.; Feng J. and Tang L. (2022a). Early renal structural changes and potential biomarkers in diabetic nephropathy. Frontiers in Physiology; 13: 1-8. DOI: 10.3389/fphys.2022.1020443

Liu X.; Jiang L.; Li Y.; Huang Y.; Hu X.; Zhu W.; et al. (2022b). Wogonin protects glomerular podocytes by targeting Bcl-2-mediated autophagy and apoptosis in diabetic kidney disease. Acta Pharmacologica Sinica; 43(1): 96-110. DOI: 10.1038/s41401-021-00721-5

Misra M. and Aiman U. (2012). Alloxan: An unpredictable drug for diabetes induction? Indian Journal of Pharmacology; 44(4): 538-539. DOI: 10.4103/0253-7613.99348

Montes S.; Juárez-Rebollar D.; Nava-Ruíz C.; Sánchez-García A.; Heras-Romero Y.; Rios C.; et al. (2015). Immunohistochemical study of Nrf2-antioxidant response element as indicator of oxidative stress induced by cadmium in developing rats. Oxidative Medicine and Cellular

Longevity; 570650: 1-9. DOI: 10.1155/2015/570650

Neutel C.; Wesley C.; Van Praet M.; Civati C.; Roth, L.; De Meyer G.; et al. (2023). Empagliflozin decreases ageing-associated arterial stiffening and vascular fibrosis under normoglycemic conditions. Vascular Pharmacology; 152: 107212. DOI: 10.1016/j.vph.2023.107212

Palmer B. and Clegg D. (2023). Kidney-Protective Effects of SGLT2 Inhibitors. Clinical Journal of the American Society of Nephrology; 18(2): 279-289. DOI: 10.2215/CJN.09380822

Rask-Madsen C. and King G. (2013). Vascular complications of diabetes: mechanisms of injury and protective factors. Cell Metabolism; 17(1):20-33. DOI: 10.1016/j.cmet.2012.11.012

Rayego-Mateos S.; Morgado-Pascual J.; Opazo-Ríos L.; Guerrero-Hue M.; García-Caballero C. and Vázquez-Carballo C. (2020). Pathogenic pathways and therapeutic approaches targeting inflammation in diabetic nephropathy. International Journal of Molecular Sciences; 21(11): 1-43. DOI: 10.3390/ijms21113798

Roger E.; Boutin L. and Chadjichristos C. (2022). The role of connexin 43 in renal disease: Insights from in vivo models of experimental nephropathy. International Journal of Molecular Sciences; 23(21): 13090. DOI: 10.3390/ijms232113090

Suvarna S.; Layton C. and Bancroft J. (2012). Bancroft’s theory and practice of histological techniques (7th ed.). New York, NY: Elsevier Health Sciences, Churchill Livingstone. (Chapters 10–12, 18, 22; pp. 179–244, 381–426, 497–542).

Viana D.; Alladagbin D.; Dos-Santos W. and Figueira C. (2022). A comparative study of human glomerular basement membrane thickness using direct measurement and orthogonal intercept methods. BMC Nephrology; 23(1):1-7. DOI: 10.1186/s12882-021-02634-1

Williams J.; Murphy S.; Wu W.; Border J.; Fan F. and Roman R. (2022). Renoprotective effects of empagliflozin in type 1 and type 2 models of diabetic nephropathy superimposed with hypertension. Geroscience; 44(6): 2845-2861. DOI: 10.1007/s11357-022-00610-7

Yang J. and Liu Z. (2022). Mechanistic pathogenesis of endothelial dysfunction in diabetic nephropathy and retinopathy. Frontiers in Endocrinology (Lausanne);13: 1-19. DOI: 10.3389/fendo. 2022. 816400

Yang, Q., Deng, L., Feng, C., Wen, J. (2024). Comparing the effects of empagliflozin and liraglutide on lipid metabolism and intestinal microflora in diabetic mice. PeerJ; 12: e17055. DOI: 10. 7717/peerj.17055.

Yuan Y.; Sun H. and Sun Z. (2017). Advanced glycation end products (AGEs) increase renal lipid accumulation: a pathogenic factor of diabetic nephropathy (DN). Lipids in Health and Disease; 16(1): 126-135. DOI: 10. 1186/s12944-017-0522-6